

# The Mechanism of Lift and Pitching Moment Reversal following an Actuator Burst over a Stalled Airfoil

Xuanhong An<sup>1†</sup>, and David R. Williams<sup>2</sup>

<sup>1</sup>Aerospace Engineering Department, San Jose State University, CA, 95192, USA

<sup>2</sup>Department Mechanical, Materials and Aerospace Engineering, Illinois Institute of Technology, IL, 60616, USA

(Received xx; revised xx; accepted xx)

The experiment of separated flow response to a single-burst actuation over a 2-D NACA-0009 airfoil at  $12^\circ$  angle of attack was conducted. The mechanism of the lift and pitching moment reversal following the single-burst actuation was studied. A spatially localized region of high pressure caused by a vortices-induced downwash is responsible for the lift and pitching moment reversal. Proper orthogonal decomposition (POD) of the flowfield shows that mode 2 shares a similar structure that produces the downwash and is responsible for the lift and pitching moment reversal. On the other hand, POD mode 1, which represents the direction and strength of the reverse flow on the suction side of the airfoil is responsible for the lift enhancement.

**Key words:** Authors should not enter keywords on the manuscript, as these must be chosen by the author during the online submission process and will then be added during the typesetting process (see <http://journals.cambridge.org/data/relatedlink/jfm-keywords.pdf> for the full list)

## 1. Introduction

Flow separation (also referred to as stall) is known for degrading the performance of fluid dynamic systems such as aircraft, helicopters and wind turbines, where wings play an important role. The separated flow on the suction side of an airfoil leads to a significant lift reduction while the drag increases dramatically. For this reason, a lot of work has been carried out to explore the techniques to reattach the separated flow on a stalled wing. Since the high-speed flow often starts to detach the suction side of the airfoil in the vicinity of the leading edge, it is natural to place the actuators close to the leading edge to excite the unstable modes in the separated flow Greenblatt & Wygnanski (2000a).

In order to achieve optimal performance, leading-edge actuation (excitation) has been studied for decades for flow separation control. These studies involve a broad range of types of actuators such as synthetic jet actuators (Glezer & Amitay 2002), plasma actuators (Corke *et al.* 2007), combustion actuators (Crittenden *et al.* 2001) and periodic blowing/suction actuators (Seifert *et al.* 1993) (Williams *et al.* 2009a). For instance, the effect of periodic blowing frequency on time-averaged lift enhancement have been

† Email address for correspondence: xuanhong@princeton.edu

studied substantially (Greenblatt & Wygnanski 2000*b*) (Müller-Vahl *et al.* 2016) (Raju *et al.* 2008), where pneumatic actuators are used. More interestingly, Glezer & Amitay (2002) investigated burst-mode actuation and reported that the burst-mode actuation is more efficient compared to other types of actuation in terms of time-averaged lift enhancement, because it utilizes the inherent instability in the fluid. However, despite the detailed flowfield analysis, these studies focus on the actuators' performance in terms of the time-averaged quantities (e.g. time-averaged lift).

In the cases where we want to actively control the flow separation (Williams *et al.* 2009*b*) in a time-varying manner (e.g. unsteady flow separation), the dynamic characteristics of the actuators become rather important. In fact, Kerstens *et al.* (2011) suggested that the bandwidth of the unsteady flow separation control is primarily limited by the time response of the actuators. Here, the time response is characterized by the time delay of the aerodynamic loads (e.g. lift) variation in response to particular input (e.g. step input) (Cattafesta III & Sheplak 2011). Therefore, studying the actuation delay is important for controlling the unsteady flow separation including actuator design.

In recent studies, An *et al.* (2016) and An *et al.* (2020) successfully modeled the actuator delay with low-order models on a stalled wing when a time-varying leading-edge actuation is used to control the separated flow. However, in order to improve the actuator design, being able to identify the low-order mathematical representation of the actuator delay is not enough, more comprehensive studies on the flow physics behind the actuation delay are needed.

The dynamic response of separated flow to leading-edge actuation has been carried out by several scholars. Amitay & Glezer (2006) investigated the time evolution of separated flow following a step input modulated on a sequence of burst signals. They found that the lift declines initially following the rising edge of the step input prior to the lift enhancement taking over. Later on, they (Amitay & Glezer 2006) conducted a similar experiment using impulse-like leading-edge actuation and found that the initial decline of the lift behaves similarly compared to that in the step input case. The initial decline of the lift is referred to as 'lift reversal' by Williams & King (2018) and they suggested that this minimum phase behavior produces a right half-plane zero that limits control bandwidth (Skogestad & Postlethwaite 2005). Given the fact that the lift reversal in the step input cases is the same as it is in the impulse input cases, investigating the impulse input is sufficient to understand the mechanism of the lift reversal. On the other hand, (An *et al.* 2017) also found a pitching moment reversal, which behaves very similar to the lift reversal following a burst mode actuation.

In addition, Williams & King (2018) reported that in flow separation control with burst-mode actuation, the inherent time delay (lift reversal) is due to the nature of the separated flow and independent of the actuators. In their work, by comparing the lift response to the actuation from different actuators including zero-net-mass-flux (ZNMF) actuators, combustion actuators, and Lorentz force actuators, they found very similar lift reversal following an impulse actuation regardless of the type of actuators. Meanwhile, a similar left reversal is also observed by Zong *et al.* (2018) using plasma actuators.

In this paper, we intend to study the mechanism of lift and pitching moment reversal following an impulse (single-burst) input to ZNMF actuators over a NACA-0009 airfoil at  $12^\circ$  angle of attack. It is important to point out that first, it has been mentioned earlier that the lift and pitching moment reversal following impulse actuation shares the same trend and mechanism as it is in the step input cases, second, the lift and pitching moment reversal is independent of the types of actuators as long as the actuation is meant to excite the instability of the separated flow. Therefore, the findings in this paper

also apply to step (as well as other time-varying) input cases and other types of actuators (e.g. combustion actuators, plasma actuators).

The remaining of this paper is arranged as follows. A detailed description of the experimental setup is given in section 2. Section 3 briefly discusses the flowfield evolution associated with the lift and pitching moment variation following the single-burst actuation. In section 4 a study of the mechanism behind the lift and pitching moment reversal is carried out using two methods. In the first method, we investigate the lift and pitching moment reversal by connecting the flowfield with its associated lift, pitching moment and pressure measurements. In the second method, we perform Proper Orthogonal Decomposition (POD) on the flowfield to identify the flow structure that is responsible for the lift and pitching moment reversal. The conclusion is given in section 5.

## 2. Experimental Setup

The experiments were conducted in the Andrew Fejer Unsteady Flow Wind Tunnel at Illinois Institute of Technology. The wind tunnel has cross-section dimensions  $600mm \times 600mm$ . The right-hand coordinate system is defined with the origin at the leading edge of the wing and the x-axis in the flow direction, the y-axis pointing upward, and the z-axis pointing in the direction of the left side of the wing. A nominally two-dimensional NACA0009 wing with a wingspan  $b = 596mm$  and chord length  $c = 245mm$  was used as the test article that is shown in figure 1. The freestream speed was  $U_\infty = 3m/s$ , corresponding to a convective time  $t_{convect} = c/U_\infty = 0.082s$ . Dimensionless time  $t^+$  is normalized by the convective time so that  $t^+ = t/t_{convect}$ . The chord-based Reynolds number is  $Re_c = 49,000$ . The angle of attack of the wing was fixed at  $\alpha = 12^\circ$ , at which the flow is fully separated on the suction side of the airfoil. In the remaining of this paper, the lift,  $L$  is nondimensionalized as the lift coefficient,  $C_L = \frac{L}{0.5\rho U_\infty^2 cb}$ , where  $\rho$  is the air density, the pitching moment  $M$  is nondimensionalized as the pitching moment coefficient,  $C_M = \frac{M}{0.5\rho U_\infty^2 c^2 b}$ , and the pressure  $P$  is nondimensionalized as the pressure coefficient,  $C_P = \frac{P}{0.5\rho U_\infty^2}$ .

Eight piezoelectric (zero net mass) actuators were installed in the leading edge of the wing. The slots of the actuators were located  $0.05c$  from the leading edge with an exit angle of 30 degrees from the tangent to the surface on the suction side of the wing. The dimension of each actuator orifice slot is  $2mm \times 40mm$ . A plan view of the wing is given in figure 1.

Surface pressure measurements were made with All-Sensors D2-P4V Mini transducers built into four chord-wise locations on the wing. The pressure range for these sensors is  $\pm 1$  inch of water. The four pressure sensors are shown in figure 1 as PS1 – PS4, and the corresponding pressure coefficient measurements will be denoted as  $C_{P1}$  –  $C_{P4}$  in the rest of this paper. Forces and moments were measured with an ATI, Inc. model Nano-17 force balance located inside the model at 30% of the chord, which is also the center of gravity of the wing. The reference point of the pitching moment is located at 25% of the chord.

Flowfield measurements using Particle Image Velocimetry (PIV) were obtained in the x,y plane located at  $z=0.19b$  away (indicated by the orange line in figure 1) from the centerline. The PIV data window in the x,y plane is shown in figure 2 with green color. The small red circle denotes the streamwise location of the actuators and the black dots are the locations of the pressure sensors. The time interval between the phase-averaged PIV measurements is  $0.005s$  ( $0.0625t^+$ ), which resulted in 800 phases covering  $4s$  ( $50t^+$ ).

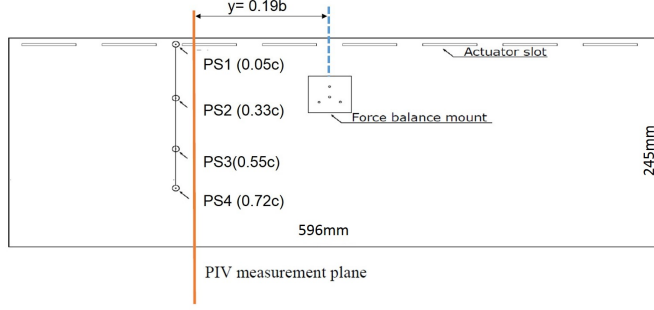


Figure 1: Plan view of the wing with NACA 0009 profile. Pressure sensor, force balance, and actuator locations are shown.

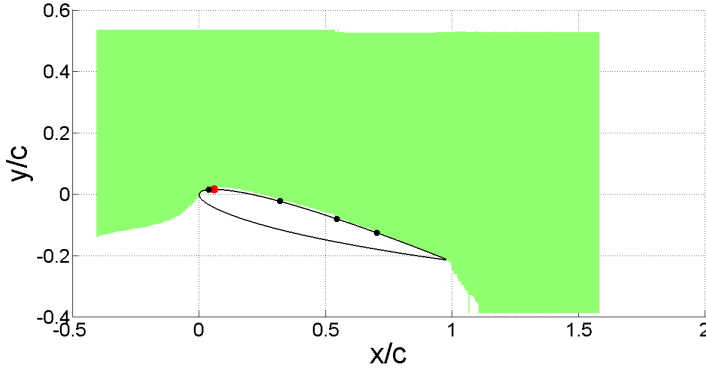


Figure 2: Side view of the wing and the PIV measurement window. Pressure sensor locations are shown by the black dots, and the actuator locations are shown by the red dot.

The phase averaging was done by averaging 100 flow field images for each phase. The initial (reference) phase corresponded to the beginning of the actuator burst signal.

To produce the maximum exit jet velocity, the ZNMF actuators are operated at their mechanical resonance frequency,  $f_r = 400\text{Hz}$  with a pulse width of  $\Delta t_p = 0.03125t^+$ , and 60 Volts ( $V$ ) amplitude. A second square wave signal was superposed on the  $400\text{Hz}$  carrier signal to create the ‘burst signal’. The burst signal width is  $\Delta t_b = 0.125t^+$ . Therefore, the actual input signal to the actuators is a short burst signal containing 4 high-frequency ( $400\text{Hz}$ ) pulses, the amplitude of the input signal,  $A = 60V$  for all the cases in the current research (figure 4). The peak exit jet velocity measured with a hot-wire anemometer at the actuator exit is  $4.9\text{m/s}$  corresponding to the peak momentum coefficient,  $C_\mu = \frac{\rho V_{jet}^2 A_{jet}}{0.5 \rho U_\infty^2 cb} = 0.01$ , where  $V_{jet}$  is the peak velocity of the actuation jet,  $A_{jet}$  is the opening area of the actuators.

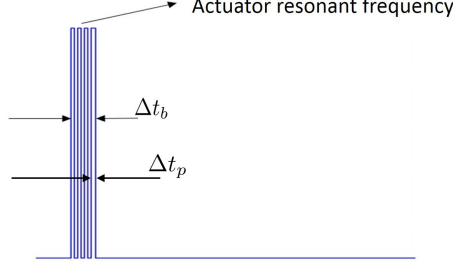
Figure 3: Single-burst actuation consists of four  $\Delta t_p$  pulses.

Figure 4: Input signal to the actuators.

### 3. Single-burst Actuation

The single-burst actuation consists of a sequence of high-frequency pulses as shown in figure 3 and it is initialized at  $0t^+$ . The corresponding lift coefficient  $C_L$  and pitching moment coefficient  $C_M$  responses are shown in figure 5. Note that we define positive  $C_M$  corresponds to a nose-up pitching moment for better presentation, although it contradicts the construction of the coordinates. The vertical dashed black lines in figure 5 indicate the critical instants on the time axes, which will be discussed in more detail later. Figure 5 exhibits the lift and pitching moment reversal, or in other words, both  $C_L$  and  $C_M$  decrease immediately following the single-burst actuation. A similar lift reversal phenomenon was identified first by Amitay & Glezer (2002). Since then the effect has been observed by numerous investigators, (Woo *et al.* June 2008; Brzozowski *et al.* 2010; Woo *et al.* 2009), and is now an established feature of the separated flow dynamics. Williams & King (2018) further concluded that the lift reversal is an inherent characteristic regardless of the types of actuators or actuation.

Figure 5c shows that both  $C_L$  and  $C_M$  reach their minima at  $1.4t^+$  during the lift and pitching moment reversal. Following the lift reversal, the  $C_L$  reaches its maximum at  $2.8t^+$  (figure 5d), the maximum  $C_L$  increment is about 30% of its undisturbed baseline value. In contrast to the  $C_L$  variation, there is no significant increase in  $C_M$  above the baseline during the entire process (figure 5). After  $4t^+$ , as it can be seen in figure 5e and figure 5f both  $C_L$  and  $C_M$  start to return to their baseline undisturbed condition. However, it takes longer for  $C_L$  to relax compared with  $C_M$ .

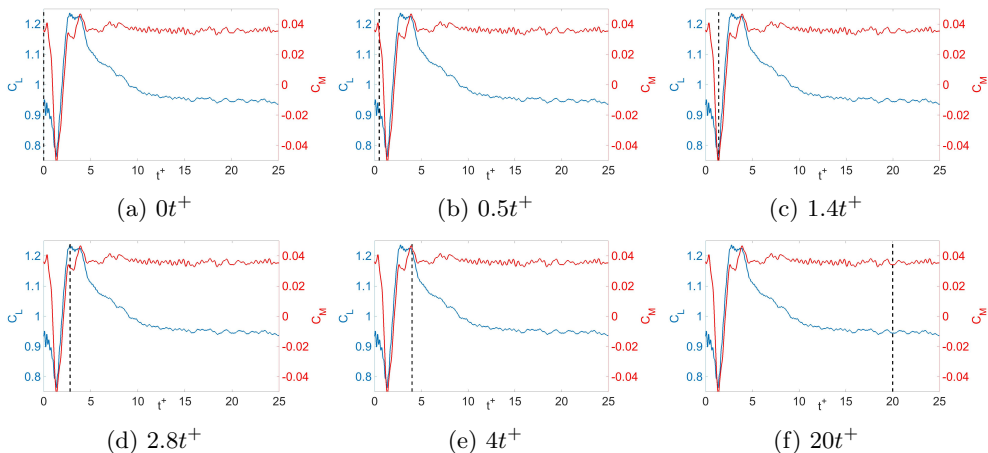


Figure 5: Phase-averaged  $C_L$  (blue) and  $C_M$  (red) variation following a single-burst actuation that is initiated at  $0t^+$ . The solid blue line denotes  $C_L$ , the solid red line denotes  $C_M$  and the dashed black line indicates the time instant correlated to each flowfield snapshot in figure 6.

The corresponding velocity field and streamline at the critical time instants following the single-burst actuation are shown in figure 6 with respect to the time instants marked by the dashed black lines in figure 5. In this figure, the color corresponds to velocity magnitude. Referring to the velocity field prior to the burst, the baseline flow on the suction side is fully separated at  $\alpha = 12^\circ$  angle of attack (figure 6a). The single-burst actuation was initiated at  $0t^+$  and lasted for  $0.12t^+$ . The beginning of the reattachment process can be seen at  $0.5t^+$  at  $x/c = 0.2$  from the leading edge (figure 6b). The reattachment produces a “kink” in the shear layer that divides the new ‘reattached’ flow from the ‘old’ separated flow region. The reattached region grows with time as the kink convects downstream from the leading edge towards the trailing edge as shown in figure 6b to figure 6d. The maximum flow reattachment occurs when the kinked region of the shear layer reaches the trailing edge at  $2.8t^+$  (figure 6d). At this time, the lift coefficient also reaches its maximum (figure 5d), which agrees with Rival’s observations (Rival *et al.* 2014). After  $4t^+$ , the lift coefficient begins to decrease as the flowfield gradually relaxes to its original baseline state. This relaxation process is exhibited in figure 6e and figure 6f, and it takes about  $10t^+$ . Brzozowski *et al.* (2010) described much of the same behavior when using combustion-based pulsed actuators on a NACA 4415 cambered wing.

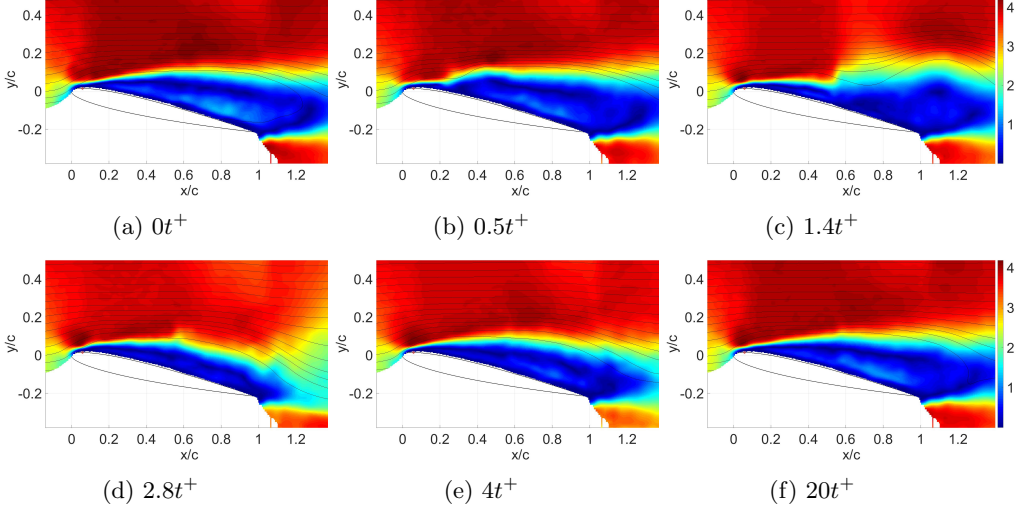


Figure 6: Phase-averaged velocity magnitude ( $\sqrt{U^2 + V^2}$ ) and streamline time sequence plots following a single-burst actuation that is initiated at  $0t^+$ , where  $U$  is the horizontal velocity along  $x$  and  $V$  is the vertical velocity along  $y$ . The color indicates the velocity magnitude and the black lines are showing the streamline. The red circle on the leading edge denotes the streamwise location of the actuators. The flow direction is from left to right.

#### 4. The mechanism of $C_L$ , $C_M$ reversal

The mechanism behind the lift and pitching moment reversals is important to be understood because this is the cause of the non-minimum phase behavior that limits control bandwidth.

##### 4.1. The relation between $C_L, C_M$ , Pressure and the flowfield

By examining the vortex structure and surface pressure evolution, we intend to gain some insight into the physics of the lift and pitching moment reversal. The methodology here is that we will first analyze the relation between lift, pitching moment and the pressure, and then analyze the relation between the surface pressure and the flowfield.

The time series data of the increments,  $\Delta C_P$ ,  $\Delta C_L$  and  $\Delta C_M$  are shown in figure 7. Here, " $\Delta$ " denotes the value in the actuated cases relative to the non-actuated baseline. Note that the vertical axis on figure 7a is " $-\Delta C_P$ " for a easier comparison with  $\Delta C_L$  and  $\Delta C_M$  (figure 7b). The pressure response to the single-burst actuation was investigated at four chordwise locations. It can be seen in figure 7a that the pressure at locations PS2, PS3, and PS4 follows a similar trend after a burst disturbance from the actuator is initiated. The more important observation is that the pressure on these three pressure sensors shows the reversal-like phenomenon, which is very similar to the lift/pitching moment reversal shown in figure 7b, there is an approximately  $0.6t^+$  constant time delay between the minima on the pressure sensors due to the convection of the disturbance. It is also worth of noting that the first pressure signal on PS1 does not follow the same pattern as the other pressure sensors, because it is located upstream of the actuator.

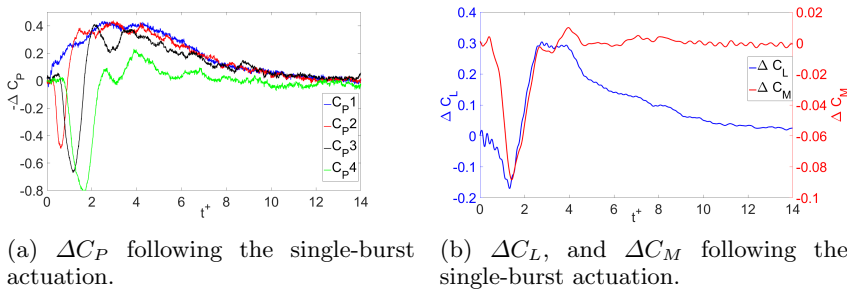
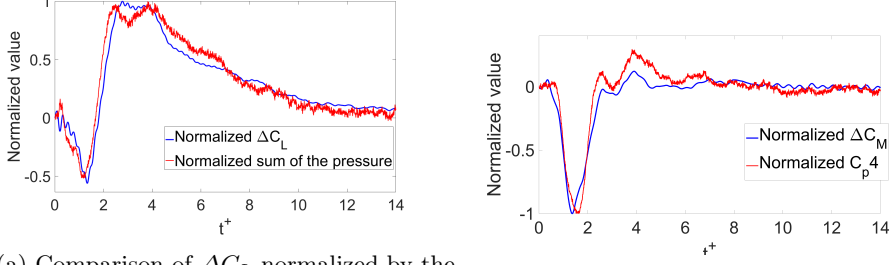


Figure 7: Lift coefficient increment and pitching moment coefficient increment measured by the force transducer, and pressure coefficient increments measured by the four pressure sensors.

To better visualize the relation between  $\Delta C_L$  and  $\Delta C_P$ , a comparison of  $\Delta C_L$  normalized by its maximum (blue) and the sum of  $\Delta C_P$  on all pressure sensors normalized by its maximum is plotted in figure 8a (red). It is obvious that  $\Delta C_L$  closely follows the trend of the sum of all pressure measurements. On the other hand, when both  $\Delta C_M$  and  $\Delta C_{P4}$  are normalized by their minima, we found that the trend of  $\Delta C_M$  is closely tracked by  $C_{P4}$  (figure 8b) measured by PS4, which is the closest to the trailing edge. This is because the moment arm of PS4 is the largest relative to the reference point (0.25c) of the moment measurement.

Up to now, we can conclude that the  $C_L$  and  $C_M$  reversal is a consequence of the surface pressure reversal following the initiation of the single-burst actuation. Next, we will connect the time-varying surface pressure to the vortex structure, so that we can obtain a more comprehensive picture of how the flowfield evolution contributes to the  $C_L$ ,  $C_M$  reversal.





(a) Comparison of  $\Delta C_L$  normalized by the maximum lift increment, and the sum of the all 4 pressure measurements normalized by the maximum.

(b) Comparison of the normalized  $\Delta C_M$  and the normalized  $C_{P4}$ .

Figure 8:  $\Delta C_L$ ,  $\Delta C_M$  and  $\Delta C_P$  normalized by their respective maxima.

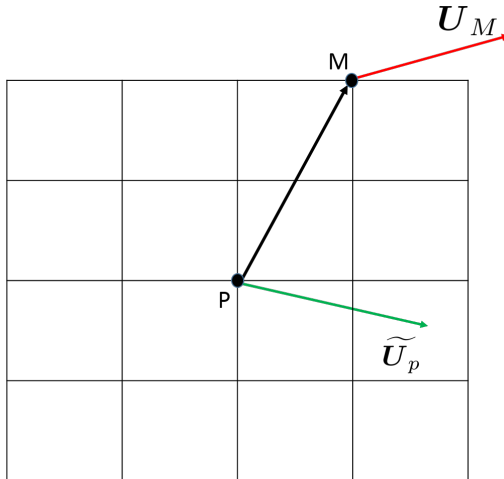
To study the flow structure associated with the lift and pitching moment reversal, a method following Graftieaux *et al.* (2001) is used to calculate the vortex strength. In Graftieaux *et al.* (2001)'s work, a Galilean invariant vortex strength  $\Gamma$  in the flow was calculated using the local swirling velocity and the spatial vector relative to the center point of the computational domain. To reduce the noise in the measured flow field, a local averaging method was used. The calculation of the vortex strength is shown as follow,

$$\Gamma(p) = \frac{1}{N} \sum_S [\mathbf{PM} \wedge (\mathbf{U}_M - \widetilde{\mathbf{U}}_p)] \cdot \mathbf{Z} \quad (4.1)$$

where  $\mathbf{PM}$  is the spatial vector from the center point  $P$  of the computational area to each individual point  $M$  surrounding  $P$  in the computational area  $S$ .  $N$  is the number of points in the surrounding area.  $\mathbf{U}_M$  is the velocity at the point  $M$ .  $\widetilde{\mathbf{U}}_p$  is the mean velocity in the area  $S$  and  $\mathbf{Z}$  is the unit vector normal to the measurement plane. In the 2-D case, Eq. 4.1 becomes

$$\Gamma(p) = \frac{1}{N} \sum_S [\mathbf{PM} \wedge (\mathbf{U}_M - \widetilde{\mathbf{U}}_p)] \quad (4.2)$$

The computational domain of  $\Gamma$  at the spatial point  $P$  is sketched in figure 9.

Figure 9: The sketch of the  $\Gamma$  computational area.

To better visualize the vortex structure, the Galilean invariant  $\Lambda_2$  criterion (Jeong & Hussain 1995) was used to identify the vortex boundary. The vortex strength  $\Gamma$  is only shown inside the vortex boundary identified by  $\Lambda_2$ . A brief description of  $\Lambda$  calculation is given here. Taking the gradient of Navier-Stokes equations, the symmetric part without unsteady and viscous effects is

$$\Omega^2 + S^2 = -\frac{1}{\rho} \nabla (\nabla P) \quad (4.3)$$

where  $S = (J + J^T)/2$ ,  $\Omega = (J - J^T)/2$  and  $J$  is the velocity gradient tensor. The tensor  $\Omega^2 + S^2$  is the corrected Hessian of pressure. The vortex core can be defined as a connected region with two negative eigenvalues ( $\Lambda_2 < 0$ ) of tensor  $\Omega^2 + S^2$ . In our case, ( $\Lambda_2 < -100$ ) is used to reduce the number of the small vortices that are caused by the turbulence and measurement noise.

The vortex structures in figure 10 are plotted at the 'critical' instants when  $C_L$  reaches its maximum and minimum, the downwash (which will be discussed in more detail later) impinges on each pressure sensor as well as the instants right before the actuation is initiated and after the flow is fully relaxed. The vortex structure at  $0t^+$  (figure 10a) shows a group of clockwise rotating vortices (blue) above the airfoil denoting the separated boundary layer. The counterclockwise rotating vortices (red) in the vicinity of the trailing edge indicate the trailing-edge vortex (TEV). As shown in figure 10b, the single-burst actuation excites the instability of the flowfield and the shear layer rolls up into two clockwise rotating vortices. The upstream part forms a new leading-edge vortex that bonds to the suction side of the airfoil. We will call this vortex the newly established leading-edge vortex or its abbreviation NELEV. The downstream portion of the shear layer rolls up into another vortex which eventually detaches from the airfoil. The previously discussed 'kink' in the shear layer is at the interface between the two vortices. The size of the downstream vortex grows continuously before it completely detaches from the airfoil (figure 10c to 10e). This vortex is referred to as the detached leading-edge vortex (DLEV). At  $2.8t^+$  (figure 10g), both the DLEV and the counter-clockwise rotating TEV have detached from the airfoil. The flow becomes less separated than the baseline separated flow, and the resulting flow leaves the trailing edge smoothly. The reattachment point reaches the trailing edge at this time, and the lift increment reaches

its maximum as previously shown in figure 6d and figure 5d. Finally, as expected, at  $20t^+$  after the actuation (figure 10h) the flow returns to the original baseline state.

The NELEV together with DLEV in figure 10 produces a downward flow (downwash) that causes the pressure reversal at each pressure sensor following the burst actuation. The location, where the downwash impinges on the suction side surface of the wing is shown in figure 10 b-e with red circles. At  $0.7t^+$  after the firing of the burst (figure 10b), the downwash flow is impinging on PS2, when this pressure sensor is showing maximum pressure reading (figure 7). Similarly, the peak in the pressure reversal occurs at PS3 and PS4 (figure 10c and figure 10e) when the downwash impinges on them.

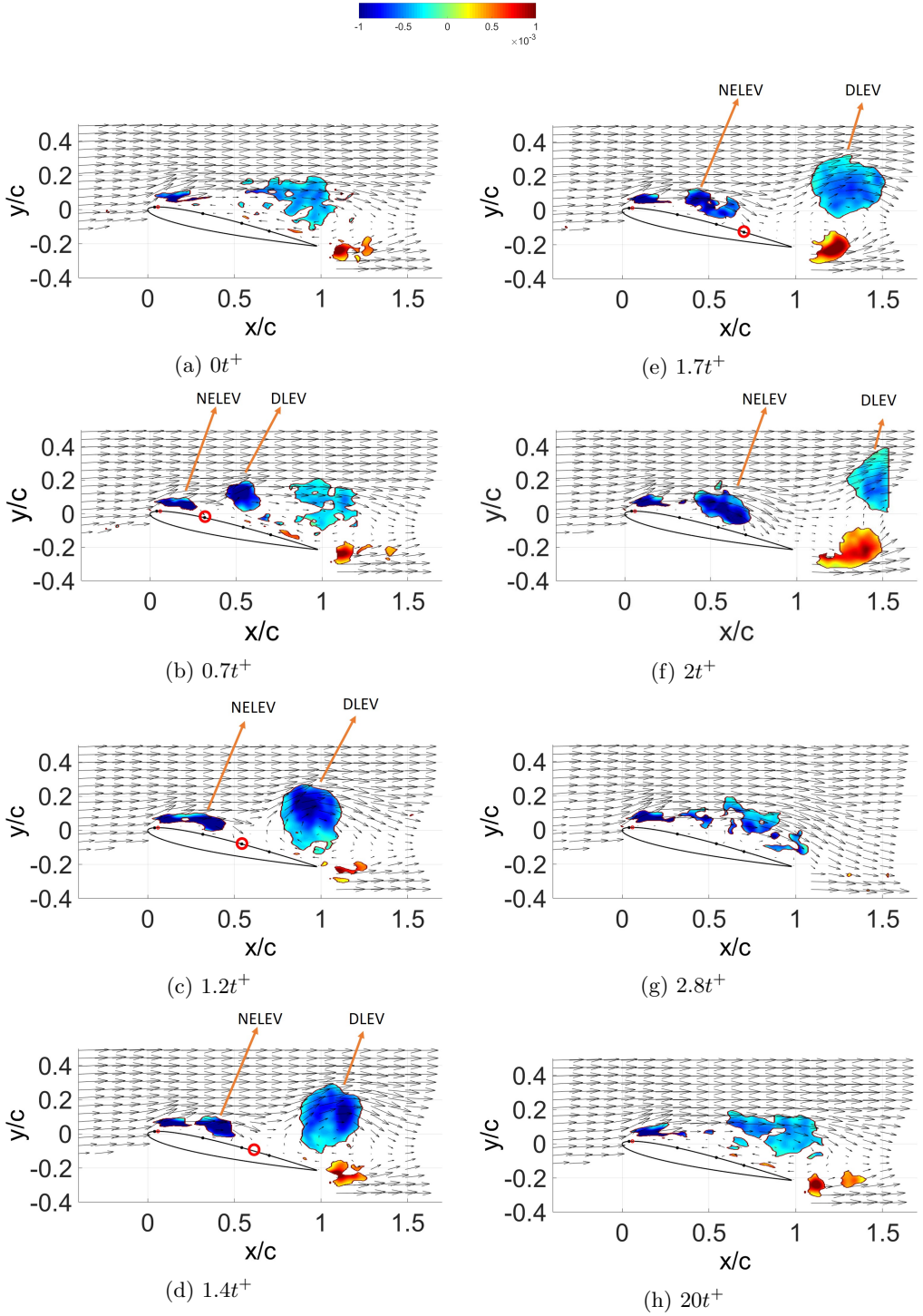


Figure 10: Vorticity maps and velocity vectors following a single burst from the actuator. The red circles denote the location where the downwash impacts the wing. The red dot close to the leading-edge indicates the location of the actuators, and the black dots show the location of the pressure sensors. The plots from a to h represent baseline ( $0t^+$ ), maximum pressure on PS2 ( $0.7t^+$ ), maximum pressure on PS3 ( $1.2t^+$ ), minimum  $C_L$  ( $1.4t^+$ ), maximum pressure on PS4 ( $1.7t^+$ ), vortices shed from the wing ( $2t^+$ ), maximum  $C_L$  ( $2.8t^+$ ) and the baseline ( $20t^+$ ).

Therefore, by combining the results of the  $\Delta C_L$  and  $\Delta C_M$  measurements, the surface pressure measurements (figure 7 and figure 8a) and the vortex structure of the flowfield (figure 10), we conclude that the formation of the vortices, DLEV and NELEV produces a downwash that impinges on the suction side of the airfoil and convects downstream. This downwash contributes to a local pressure reversal and as a consequence, the sequence of local pressure reversal leads to the lift and pitching moment reversal following the single-burst actuation.

#### 4.2. Proper Orthogonal Decomposition (POD) of the flow field

Next, we apply the Proper Orthogonal Decomposition (POD) to the flowfield snapshots following the single-burst actuation to gain additional insight into the modes that are responsible for the lift and pitching moment reversal. This is inspired by the experiment conducted by Monnier *et al.* (2016). They reported that the negative temporal coefficient of the second POD mode correlates with the lift coefficient variation following a single-burst actuation.

The POD method can reduce a large number of interdependent variables to a much smaller number of independent modes while retaining as much as possible the variation in the original variables (Kerschen *et al.* 2005).

$$v(x, t) = \sum_{i=1}^{\infty} a_i(t) \phi_i(x) \quad (4.4)$$

in Eq. 4.4,  $a_i$  is the time-dependent temporal coefficient and  $\phi_i(x)$  is the POD basis function. Singular Value Decomposition (SVD) (Kerschen *et al.* 2005) is performed on both horizontal and vertical velocity components obtained from the PIV measurements.

For any given ( $m \times n$ ) matrix  $X$

$$X = USV^T \quad (4.5)$$

where  $U$  is an ( $m \times m$ ) orthonormal matrix containing the left singular vectors,  $S$  is a ( $m \times n$ ) pseudo-diagonal and semi-positive definite matrix with diagonal elements  $\delta_i$ , and  $V$  is an ( $n \times n$ ) orthonormal matrix containing the right singular vectors. There are physical meanings for each term from the SVD. The matrix  $U$  represents the spatial distribution of velocity within each POD mode,  $V$  contains the temporal coefficients for each mode, and the pseudo-diagonal elements of  $S$  denote the energy level for the modes, in which the energy is descending with increasing of the mode number.

The energy contained in each mode is normalized by mode 0 and plotted in figure 11. It shows that about 84% of the disturbed flow energy (with mode 0 subtracted from the flowfield) is contained in mode 1 and mode 2, which means that mode 1 and mode 2 can reconstruct a flowfield retaining most of the energetic structures in the disturbed flow.

The corresponding basis functions and the temporal coefficients for the first three modes are plotted in figure 12. Mode 0 (figure 12a) shows the flow structure that is very similar to the baseline separated flow. Figure 12b shows that mode 0 almost remains unchanged with time. The temporal coefficient of mode 0 is always above 0 which means the directions of the velocity vectors in figure 12a are preserved. Mode 1 shown in figure 12c is related to the reverse flow along the airfoil that causes flow separation. The temporal coefficient (figure 12d) of this mode goes negative  $1.2t^+$  after the burst is initiated, which implies that the velocity vectors in this spatial mode flip their directions and thus, contribute to flow reattachment thereafter until its fully relaxed. Mode 2 shown in figure 12e represents the DLEV downstream of the trailing edge, NELEV on the surface of the airfoil and the associated downwash impinging on the upper surface of the airfoil

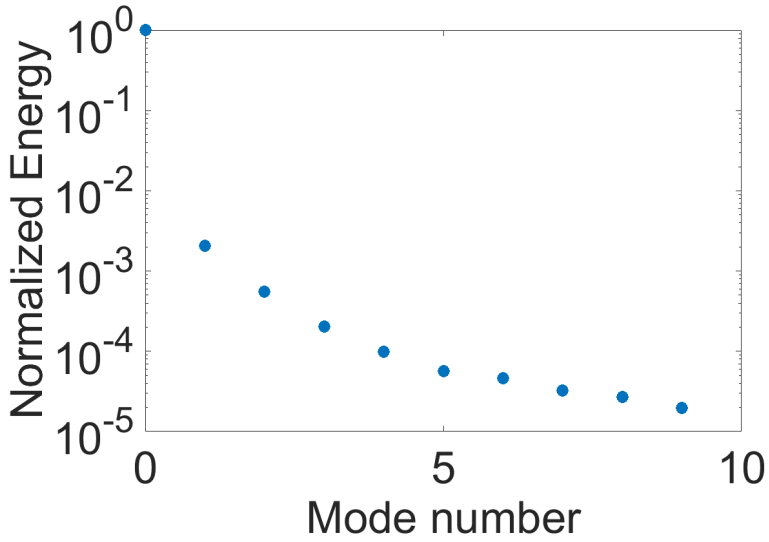


Figure 11: Energy distribution versus POD mode number.

at the vicinity of PS4. The temporal coefficient of this mode (figure 12f) goes above 0 following the burst until  $2.5t^+$ , which preserves the directions of the velocity vectors in figure 12e. This implies that mode 2 is related to the  $C_L$  and  $C_M$  reversal. Next, we will make a direct comparison between the  $C_L$ ,  $C_M$  and the POD modes.

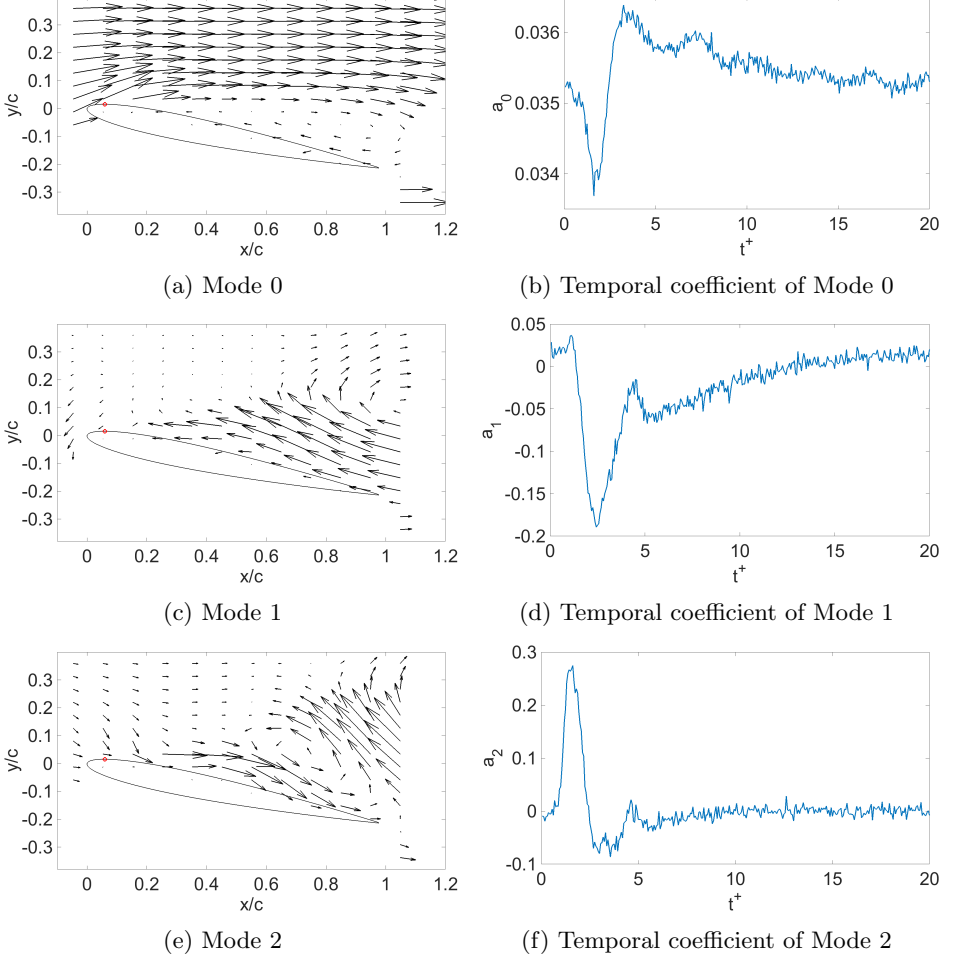


Figure 12: Comparison of the first four spatial POD modes and their corresponding temporal coefficients.

The sum of the negative temporal coefficients of mode 1 and mode 2 is plotted in figure 13a. Note that all the time coefficients of the POD modes are normalized by the minimum of the  $\Delta C_L$  or  $\Delta C_M$  respectively. Comparing  $\Delta C_L$  to the combination of mode 1 and mode 2,  $a_1 \cdot \delta_1 + a_2 \cdot \delta_2$ , the negative temporal coefficient of mode 1 and mode 2 combination tracks the  $\Delta C_L$  very well (especially for the lift reversal), other than mode 2 alone, reported by Monnier *et al.* (2016).

Meanwhile, the negative temporal coefficient of mode 2 alone is closely tracking the measured  $\Delta C_M$ , since this mode represents the downwash impinging on PS4 (13b), which has the longest momentum arm from the reference point. This observation again, suggests that the pitching moment reversal is caused by the downwash impinging on PS4 that is represented by POD mode 2.

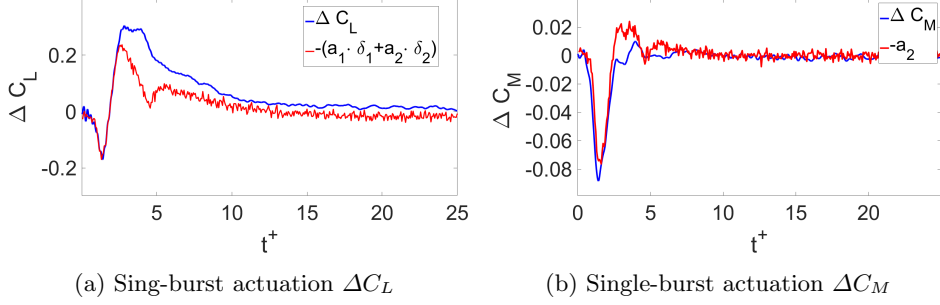
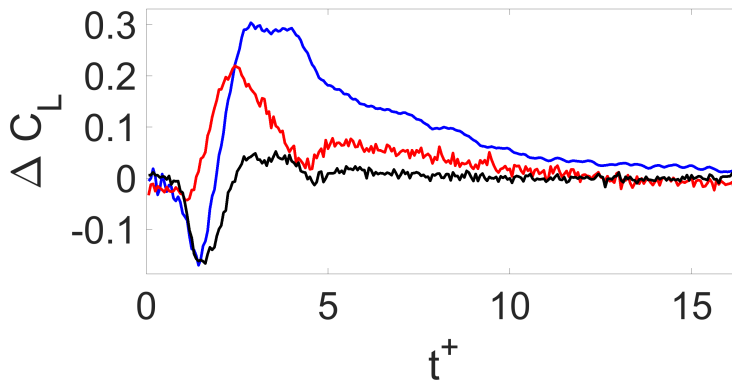


Figure 13: Comparison of aerodynamic loads and time varying coefficient of POD modes, (a) lift coefficient, (b) pitching moment coefficient.

On the other hand, since the lift reversal is tracked by the combination of mode 1 and mode 2, another direct comparison between each individual POD mode and  $\Delta C_L$  is carried out in figure 14. It shows that the negative time coefficient of mode 2 follows  $\Delta C_L$  from the initialization of the burst to  $1.2t^+$  while the time coefficient of mode 1 almost remains constant with a positive value (which indicates a reverse flow on the airfoil or in other words, flow is separated). During this time period ( $0t^+$  to  $1.2t^+$ ), the lift reversal is perfectly captured by mode 2. After  $1.2t^+$ , mode 2 starts to deviate from  $\Delta C_L$  only because the time coefficient of mode 1 starts to vary and goes up. Therefore, the good correlation between the negative coefficient of POD mode 2 and the lift reversal curve suggests that this mode is responsible for the lift reversal. In other words POD mode 2 which represents the formation of NELEV and DLEV associated with their induced downwash cause the lift reversal. In addition, the time coefficient of mode 2 is almost always equal to zero except when the lift/pitching moment reversal occurs, which suggests that this flow pattern contributes to the lift/pitching moment reversal only. On the other hand, the comparison between POD mode 1 and  $\Delta C_L$  in figure 14 suggests POD mode 1, which represents the reverse flow on the surface of the airfoil contributes to the lift enhancement.



Figure 14: POD mode 1, POD mode 2 and  $\Delta C_L$ .

## 5. Conclusion

In this work, the mechanism of the lift and pitching moment reversal following a single-burst actuation on a stalled NACA-0009 airfoil is studied experimentally. The time-evolving flow structure, lift, pitching moment, pressure and their dynamic characteristics are analyzed. The maximum lift and pitching moment reversal is observed at the vicinity of  $1.4t^+$  after the initiation of the single-burst, and the maximum lift increment occurs at  $2.8t^+$ , when the flow is reattached. We observed that following the initiation of the actuation, there is a downwash impinging on the suction side of the wing that moves with the clockwise rotating large-scale leading-edge vortices. This results in a pressure reversal and thus, leads to the lift and pitching moment reversal before the DLEV convects into the wake. A further POD analysis shows that 84% of the disturbed kinetic energy is retained in mode 1 and mode 2. The combined negative temporal coefficients of POD mode 1 and mode 2 track the lift coefficient curve well, especially during the lift reversal. Comparing the time coefficient of POD mode 2 with the lift and pitching moment variation, it confirms that the flow structure representing the downwash induced by DLEV and NELEV is responsible for lift and pitching moment reversal. We also found POD mode 1 which represents the strength and direction of the reverse flow on the suction side of the airfoil is responsible for the lift enhancement. The outcome of this paper could potentially benefit the fluidic actuator design to reduce the lift and pitching moment reversal and thus, leads to faster actuation response for unsteady flow separation control.

## REFERENCES

- AMITAY, MICHAEL & GLEZER, ARI 2002 Controlled transients of flow reattachment over stalled airfoils. *International Journal of Heat and Fluid Flow* **23** (5), 690–699.
- AMITAY, MICHAEL & GLEZER, ARI 2006 Flow transients induced on a 2d airfoil by pulse-modulated actuation. *Experiments in Fluids* **40** (2), 329–331.
- AN, XUANHONG, WILLIAMS, DAVID R, ELDREDGE, JEFF D & COLONIUS, TIM 2016 Modeling dynamic lift response to actuation. In *54th AIAA Aerospace Sciences Meeting*, p. 0058.
- AN, XUANHONG, WILLIAMS, DAVID R & HEMATI, MAZIAR S 2020 A hybrid model for lift response to dynamic actuation on a stalled airfoil. *Energies* **13** (4), 855.
- AN, XUANHONG, WILLIAMS, DAVID R, DA SILVA, ANDRE F, COLONIUS, TIM & ELDREDGE, JEFF 2017 Response of the separated flow over an airfoil to a short-time actuator burst. In *47th AIAA fluid dynamics conference*, p. 3315.

- BRZOWSKI, DAN, WOO, GEORGE TK, CULP, JOHN R & GLEZER, ARI 2010 Transient separation control using pulse-combustion actuation. *AIAA journal* **48** (5), 2482.
- CATTAFESTA III, LOUIS N & SHEPLAK, MARK 2011 Actuators for active flow control. *Annual Review of Fluid Mechanics* **43**, 247–272.
- CORKE, THOMAS C, POST, MARTIQUA L & ORLOV, DMITRY M 2007 Sdbd plasma enhanced aerodynamics: concepts, optimization and applications. *Progress in Aerospace Sciences* **43** (7), 193–217.
- CRITTENDEN, THOMAS, GLEZER, ARI, FUNK, ROBERT & PAREKH, DAVID 2001 Combustion-driven jet actuators for flow control. In *15th AIAA Computational Fluid Dynamics Conference*, p. 2768.
- GLEZER, ARI & AMITAY, MICHAEL 2002 Synthetic jets. *Annual review of fluid mechanics* **34** (1), 503–529.
- GRAFTIEAUX, LAURENT, MICHARD, MARC & GROSJEAN, NATHALIE 2001 Combining piv, pod and vortex identification algorithms for the study of unsteady turbulent swirling flows. *Measurement Science and technology* **12** (9), 1422.
- GREENBLATT, DAVID & WYGNANSKI, ISRAEL J 2000*a* The control of flow separation by periodic excitation. *Progress in aerospace Sciences* **36** (7), 487–545.
- GREENBLATT, DAVID & WYGNANSKI, ISRAEL J. 2000*b* The control of flow separation by periodic excitation. *Progress in Aerospace Sciences* **36**, 487–545.
- JEONG, JINHEE & HUSSAIN, FAZLE 1995 On the identification of a vortex. *Journal of fluid mechanics* **285**, 69–94.
- KERSCHEN, GAETAN, GOLINVAL, JEAN-CLAUDE, VAKAKIS, ALEXANDER F & BERGMAN, LAWRENCE A 2005 The method of proper orthogonal decomposition for dynamical characterization and order reduction of mechanical systems: an overview. *Nonlinear dynamics* **41** (1), 147–169.
- KERSTENS, WESLEY, PFEIFFER, JENS, WILLIAMS, DAVID, KING, RUDIBERT & COLONIUS, TIM 2011 Closed-loop control of lift for longitudinal gust suppression at low reynolds numbers. *AIAA journal* **49** (8), 1721–1728.
- MONNIER, BRUNO, WILLIAMS, DAVID R, WEIER, TOM & ALBRECHT, THOMAS 2016 Comparison of a separated flow response to localized and global-type disturbances. *Experiments in Fluids* **57** (7), 1–16.
- MÜLLER-VAHL, HANNS FRIEDRICH, NAYERI, CHRISTIAN NAVID, PASCHEREIT, CHRISTIAN OLIVER & GREENBLATT, DAVID 2016 Dynamic stall control via adaptive blowing. *Renewable Energy* **97**, 47–64.
- RAJU, RENI, MITTAL, RAJAT & CATTAFESTA, LOUIS 2008 Dynamics of airfoil separation control using zero-net mass-flux forcing. *AIAA journal* **46** (12), 3103.
- RIVAL, DAVID E, KRIEGSEIS, JOCHEN, SCHAUB, PASCAL, WIDMANN, ALEXANDER & TROPEA, CAMERON 2014 Characteristic length scales for vortex detachment on plunging profiles with varying leading-edge geometry. *Experiments in fluids* **55** (1), 1660.
- SEIFERT, A, BACHAR, T, KOSS, D, SHEPSHELOVICH, M & WYGNANSKI, I 1993 Oscillatory blowing: a tool to delay boundary-layer separation. *AIAA journal* **31** (11), 2052–2060.
- SKOGESTAD, SIGURD & POSTLETHWAITE, IAN 2005 *Multivariable Feedback Control: Analysis and Design*. Hoboken, NJ, USA: John Wiley & Sons, Inc.
- WILLIAMS, DAVID R & KING, RUDIBERT 2018 Alleviating unsteady aerodynamic loads with closed-loop flow control. *AIAA Journal* **56** (6), 2194–2207.
- WILLIAMS, DAVID R, TADMOR, GILEAD, COLONIUS, TIM, KERSTENS, WESLEY, QUACH, VIEN & BUNTAIN, SETH 2009*a* The lift response of a stalled wing to pulsatile disturbances. *AIAA J* **47** (12), 3031–3037.
- WILLIAMS, DAVID R., TADMOR, GILEAD, COLONIUS, TIM, KERSTENS, WESLEY, QUACH, VIEN & BUNTAIN, SETH 2009*b* Lift response of a stalled wing to pulsatile disturbances. *AIAA JOURNAL* **47**, 3034–3035.
- WOO, GEORGE, CRITTENDEN, THOMAS & GLEZER, ARI 2009 Transitory separation control over a stalled airfoil. *AIAA paper* **4281**, 2009.
- WOO, GEORGE T. K., CRITTENDEN, THOMAS M. & GLEZER, ARI June 2008 Transitory control of a pitching airfoil using pulse combustion actuation. *4th Flow Control Conference, AIAA Paper 2008-4324*.
- ZONG, HAOHUA, VAN PELT, TIMO & KOTSONIS, MARIOS 2018 Airfoil flow separation control

with plasma synthetic jets at moderate reynolds number. *Experiments in Fluids* **59** (11), 1–19.